Surface circulation in the Gulf of Thailand from remotely sensed observations: seasonal and interannual timescales

Arachaporn Anutaliya[1]

[1]Institute of Marine Science, Burapha University, Chonburi, Thailand

Correspondence: Arachaporn Anutaliya (arachaporn.an@go.buu.ac.th)

Abstract. The Gulf of Thailand (GoT), a shallow basin located in the western equatorial Pacific, undergoes highly-variable wind influences on both seasonal and interannual timescales. On seasonal timescale, the Asian monsoon prevails, dominating the circulation pattern. The most dominant complex empirical orthogonal function of the Gulf of Thailand (GoT) current explains 28% of the total variance with the phase relationship following the monsoon seasons. High current variability is observed over the upper GoT (uGoT), along the western boundary which is highly correlated with that at the southeastern entrance, and in the GoT interior. Satellite altimetry suggests that approximately 50% of the surface current variability is geostrophic set up by wind stress curl, particularly at basin-scale. Also, the study hints at the importance, to sea surface height near the coastline, of coastal trapped Kelvin waves forced by wind stress curl. Wind-driven current accounts for a significant fraction of the ageostrophic flow along the western boundary and the GoT interior; however, its effect is unclear over the uGoT. At interannual timescale, the GoT circulation is directly impacted by both El Niño Southern Oscillation (ENSO) and the Indian Ocean Dipole (IOD). Interestingly, the climate modes affect the circulation over each region of the GoT differently. The IOD highly correlates with interannual variability of current along the GoT western boundary and the southern boundary of the observing domain (8° N), while the ENSO correlates with that in the interior. Over the uGoT, both climate modes explain similar percentage of the interannual current variability.

1 Introduction

The Gulf of Thailand (GoT) located at 6°-14° N, 98° - 106° E (Figure 1) is a shallow semi-enclosed basin with an average depth of 40 m that is largely influenced by winds on both seasonal and interannual timescales. On seasonal timescale, the Asian monsoon winds prevail producing a wet season over southeast Asia during the southwest monsoon (May to August) and a dry season during the northeast monsoon (November to February). The extreme seasonal wind and precipitation conditions influence the circulation pattern, physical seawater properties (e.g. salinity, density, hence the thermohaline circulation; Yanagi and Takao, 1998; Yanagi et al., 2001; Buranatheprat et al., 2002, 2008), and nutrients loadings (e.g. nitrate, phosphate, and ammonia) from rivers (Suvapepun, 1991; Sriwoon et al., 2008). Also, the location of the GoT which is to the west of the South China Sea (SCS) in the equatorial western Pacific Ocean provides a unique opportunity in observing the influence of both large-scale climate modes in the Pacific Ocean (El Niño Southern Oscillation: ENSO) and the Indian Ocean (Indian Ocean

25   Dipole: IOD; Saji et al., 1999) on the interannual circulation.

    Previous observational and numerical studies show that circulation in the Gulf of Thailand varies seasonally (e.g., Yanagi et al., 2001; Buranatheprat et al., 2008; Saramul, 2017; Buranatheprat et al., 2002; Aschariyaphotha et al., 2008; Saramul and Ezer, 2014). A series of 6 hydrographic cruises over October 2003 – July 2005 in the upper GoT (uGoT; north of 12.5° N)

30   suggest the overall cyclonic circulation during the northeast monsoon (November – February; Buranatheprat et al., 2008) in agreement with numerical studies that accounts for tidal forcing, bottom friction, and river runoffs (Buranatheprat et al., 2002; Saramul and Ezer, 2014). Still, both numerical simulations are forced by spatially uniform reanalysis wind products, which is likely not representing the actual GoT wind field (Yanagi and Takao, 1998). The numerical studies also suggest the dominance of contrasting anticyclonic circulation in the uGoT during the southwest monsoon (May – August). Results from hydrographic

35   surveys in May 2004 and July 2005 do not show a clear dominant circulation pattern during this period (Buranatheprat et al., 2008). High spatial-resolution coastal radar of the monthly-mean surface current during both of the southwest (June 2015) and northeast monsoon (February 2015) reveals complex circulation pattern in the uGoT, although the circulations during the two seasons are not distinctly different (Saramul, 2017). The study suggests an overall cyclonic circulation in the northern part of the uGoT (north of 12.8°-12.9° N) and anticyclonic circulation in the southern part (south of 12.8°-12.9° N) during both

40   monsoon seasons.

    South of 12.5° N, various observational and numerical studies were conducted (Wyrtki, 1961; Yanagi and Takao, 1998; Aschariyaphotha et al., 2008; Sojisuporn et al., 2010); however, the findings are not quite consistent due to different studied periods and spatial resolution being considered. During the southwest monsoon, altimetry-based observation over the 1995 -

45   2001 period (Sojisuporn et al., 2010) shows that the circulation intensifies at the rim of the GoT with strong southward current along the western boundary of the GoT and eastward current to the south of the uGoT yielding a cyclonic circulation within 1° of the coastline. At the southeastern entrance, satellite altimetry indicates an outflow into the SCS (Sojisuporn et al., 2010). Numerical simulation assimilating measurements from the NAGA expedition in 1959-1960 (Yanagi and Takao, 1998) shows similar results, except the presence of strong northwestward flow in the mid-basin which yields a cyclonic circulation to its

50   west and an anticyclonic circulation to its east. In contrast, another numerical simulation based on Princeton Ocean Model (Aschariyaphotha et al., 2008) finds strong southeastward flow in the mid-basin and the dominance of an anticyclonic circulation over the GoT with an outflow at the southeastern entrance during the southwest monsoon. Note that Aschariyaphotha et al. (2008) allow inflow and outflow from the lateral boundaries while Yanagi and Takao (1998) do not which could contribute to the discrepancy. Still, the circulation pattern found by Aschariyaphotha et al. (2008) resembles the GoT surface velocity

55   surveyed during the NAGA expedition (Wyrtki, 1961). During the northeast monsoon, the altimetry observations and numerical simulations suggest the dominance of an anticyclonic circulation at the rim of the GoT and an inflow at the southeastern entrance (Yanagi and Takao, 1998; Aschariyaphotha et al., 2008; Sojisuporn et al., 2010). Circulation in the GoT interior is quite complex and findings from the studies do not necessarily agree. The NAGA expedition, however, shows that cyclonic circulation prevails during the northeast monsoon (Wyrtki, 1961). Still, an inflow is present at the southeastern entrance in

60   agreement with the observational and numerical studies. The inflow is found to reach the bottom at the GoT western boundary during the spring monsoon transition as cold and saline water originated in the SCS is observed there by a hydrographic survey (Yanagi et al., 2001).

    Although previous studies have recognized the role of monsoon winds on seasonal variability of the GoT circulation (e.g.,

65   Yanagi and Takao, 1998; Aschariyaphotha et al., 2008), the associated dynamics are not well understood. Therefore, this study aims to examine seasonal variability of surface circulation in the GoT and the associated dynamics by investigating the influence of geostrophic current and wind-driven Ekman current using remotely-sensed observations. The mechanisms that set up the geostrophic flow will also be discussed. In addition, interannual variability of the GoT circulation will be examined to understand the effect of ENSO and the IOD on the circulation pattern.

70

2   Datasets

    To examine circulation pattern in the GoT, the gridded Ocean Surface Currents Analyses Real-time product (OSCAR; Bonjean and Lagerloef, 2002) between 8° and 14° N, 99° and 105° E is considered (Figure 1). The product is calculated based on satellite sea surface height, wind, and water temperature from both remotely-sensed and in-situ measurements, e.g. drifters,

75   moored, and shipboard measurements etc. The resulting current is an average in the upper 30 m of the water column. The gridded OSCAR product has a resolution of 1/3° (36-37 km in the GoT) with a temporal resolution of 5 days available from 1992 to 2020. To validate the OSCAR velocity over the GoT, it is compared to tide-removed surface currents from high frequency radar system (Saramul, 2017). Generally, OSCAR velocity exhibits similar circulation pattern to the coastal-radar velocity particularly during the northeast monsoon season. Still, much more complex circulation is observed in the coastal-radar velocity

80   due to its much higher spatial resolution. The difference between OSCAR velocity and high-frequency coastal-radar velocity is the largest in the uGoT where there are only 6 OSCAR data points.

    The gridded all-satellite merged absolute dynamic topography (ADT) product is used to determine the importance of geostrophic current in the GoT and the associated mechanisms. The product is interpolated daily on a 1/4° grid (27-28 km

85   in the GoT) available over the 1993 – 2020 period (Ducet et al., 2000). As the satellite altimetry used here is in the coastal region (Figure 1), sea surface level data from 3 tide gauge stations in the GoT, which are Fort Phrachula Chomklao (FP), Ko Lak (KL), and Ko Mattaphon (KM) (Holgate et al., 2013; PSMSL, 2019), are used to validate the satellite-derived ADT. The comparisons show high correlation between the fluctuation of satellite ADT and the tide gauge sea level over the 2014-2019 period with correlation coefficients of 0.69, 0.94, and 0.88 at FP, KL, and KM, respectively. The lower correlation found at FP

90   is due to its inland location, and thus locates the farthest away from the available gridded satellite ADT (∼20 km).

To examine the effect of wind-driven Ekman current on the GoT circulation, the gridded surface vector winds Version 2
Cross-Calibrated Multi-Platform (CCMPv2) obtained from Remote Sensing Systems are used. The CCMPv2 wind product,
available from July 1987 to December 2019, has a resolution of 1/4° with a temporal resolution of 6 hours (Wentz et al., 2015).

95   The Ekman current (u_e and v_e) at each depth (z) is calculated following Alberty et al. (2019):

$$u_e(z) = \frac{\sqrt{2}}{fd} e^{z/d} \left[\tau^x \cos\left(\frac{z}{d} - \frac{\pi}{4}\right) - \tau^y \sin\left(\frac{z}{d} - \frac{\pi}{4}\right) \right], \tag{1}$$

$$v_e(z) = \frac{\sqrt{2}}{fd} e^{z/d} \left[\tau^x \sin\left(\frac{z}{d} - \frac{\pi}{4}\right) + \tau^y \cos\left(\frac{z}{d} - \frac{\pi}{4}\right) \right], \tag{2}$$

where f represents Coriolis parameter, d is thickness of the surface Ekman layer defined as $\sqrt{\frac{2A}{|f|}}$ with A being a function

100   of wind speed, τ is wind stress in the zonal (x) and meridional (y) directions. In addition, wind stress curl ($\nabla \times \tau$) is also
calculated from the CCMPv2 product.

3   Circulation in the Gulf of Thailand

The mean and variance of OSCAR surface velocity is calculated over the 2014 - 2019 period (Figure 2). Strong flow is observed
near the northern and western boundaries of the GoT and at the southeastern entrance. The mean current along the western

105   boundary is northward to the south of 12° N, but southwestward or westward to the north of 12° N indicating a convergence at
this latitude. The mean flow at the southeastern entrance is westward and southwestward transporting water from the SCS into
the GoT. The mean circulation pattern from OSCAR products generally agrees with the satellite-derived geostrophic current
(color contour in Figure 2a), except in the uGoT where OSCAR velocity products are present at only six locations. OSCAR
velocity has high variance along the entire western boundary of the GoT where most of the variability is associated with merid-

110   ional velocity and at the southeastern entrance where the variability is observed for both zonal and meridional components
(Figure 2b). Along the western boundary of the GoT, variance of ADT is also high indicating the influence of geostrophic flow.
However, the ADT variance is low at the southeastern entrance highlighting the importance of ageostrophic flow that drives
circulation into and out of the GoT.

115   To understand the variability of the GoT circulation, the mean surface velocity (quivers in Figure 2a) is removed from the
OSCAR current to calculate Complex Empirical Orthogonal Function (CEOF). Only the first 2 modes which explain 28% and
14% of the total variance are considered (Figure 3). The first mode describes an anticyclonic circulation during the southwest
monsoon and fall monsoon transition in the interior of the GoT centered at 10.5° N, 101.5° E with a strong southward flow
along the western boundary (Figure 3a-c). Flow at the southeastern entrance of the GoT is southeastward indicating the outflow

120   from the GoT into the SCS. In the uGoT where there are only 6 grid points in the middle of the region, the surface current is
westward. During the northeast monsoon and spring monsoon transition, the circulation pattern reverses. The second CEOF
mode highlights strong flow along the western boundary of the GoT with the strongest flow in the uGoT and weaker flow

toward the central and lower GoT resembling the pattern of the circulation variance (Figure 2b, 3d). Although the phase does not exhibit a distinct pattern (Figure 3f), negative phase is found between the end of southwest monsoon and early fall

125 monsoon transition (July – October) of 2016 – 2019. The negative phase indicates southward flow along the western boundary that is strongest in the uGoT area and a weak southward flow at the southeastern entrance of the GoT which could associates with river runoffs (Aschariyaphotha and Wongwises, 2012). In addition, positive phase is found during the spring monsoon transition except in 2016 indicating northward flow along the western boundary and at the southeastern entrance which could associated with the SCS inflow (Yanagi et al., 2001; Aschariyaphotha et al., 2008).

3.1 Seasonal circulation in the Gulf of Thailand

130

3.1.1 Overall description

As suggested by the dominating circulation pattern calculated from CEOF, more than one quarter of the variance in the GoT current can be explained by a simple annually reversing circulation pattern which is in-phase with the monsoon seasons (Figure 3a-c). Monthly mean current over the 2014 – 2019 period also reveals circulation pattern generally consistent to that shown by

135 CEOF1 (Figure 4a, c, e, g). The pattern describes the circulation consisting of four main regions with high variance which are the uGoT, the western boundary of the GoT, the interior of the GoT, and the southeastern entrance of the GoT. In the interior of the GoT, anticyclonic circulation is present (centered at 10.5° N, 101.5° E) in June and September, representing the southwest monsoon and fall monsoon transition respectively (Figure 4b, c). Over the uGoT, the OSCAR current shows tendency of circulation pattern in the opposite direction to that in the central GoT, i.e. cyclonic during the southwest monsoon and fall

140 monsoon transition, despite the sparse sampling locations limited to the middle part of the uGoT (Figure 2). The monthly mean surface current hints the connection between the currents along the western boundary and that at the southeastern entrance (Figure 4a, c, e, g). The current is southward along the western boundary, while that is southeastward at the southeastern entrance during the southwest monsoon and fall monsoon transition; circulations at both regions indicate flow out of the GoT. The opposite is observed during the northeast monsoon and spring monsoon transition, consistent with previous surface current

145 observation (Saramul, 2017). To understand the dynamics associated with the strong western boundary current particularly if it is related to the current at the southeastern entrance, complex correlation analysis between current along the western boundary and that over the GoT is performed. On timescales longer than 30 days, currents along the southern boundary of the domain (south of 8.5° N) gives higher correlation to the western boundary current (9.0° - 11.5° N, 99.5° - 100.2° E) compared to the rest of the GoT (Figure 5); the correlation is higher than 0.25 with the highest value of 0.57 at the entrance. The correlation

150 between the western boundary current and that along the southern boundary of the domain is significant with 95% confidence as determined by a non-parametric method where correlation coefficients are computed repeatedly (5000 times) using both of the time series that are randomly rearranged. The significant correlation strongly suggests a connection between the GoT western boundary current and the GoT inflow/outflow at the southeastern entrance through a passage to the south of 8.5° N. During the northeast monsoon and spring monsoon transition, the GoT circulation generally reverses its direction (Figure 3a).

3.1.2 Geostrophic and ageostrophic component

Satellite altimetry is used to estimate geostrophic components of the surface circulation over the GoT. Although the altimetry may include short-period contribution during the satellite over-pass, geostrophic velocity calculated from the altimetry is found to be reasonably close to the observation (Yu et al., 1995). In the Mediterranean Sea, the altimetry-derived geostrophic velocity is generally smaller than the drifter observations (Poulain et al., 2012); the error increases with the geostrophic velocity with an error of 7-17% at the velocity of 1.5 m s^{-1} (Kubryakov and Stanichny, 2013). The satellite ADT is linearly interpolated onto the 1/3° OSCAR grid. Magnitude of geostrophic current is generally comparable to that of the total current, although their directions are not perfectly aligned (Figure 4). The root-mean-square (rms) difference between the total and the geostrophic current (i.e. the estimated ageostrophic current) ranges from 0.04 to 0.11 m s^{-1} with the median ranging from 0.03 to 0.08 m s^{-1}. The largest mismatch occurs in the uGoT and along the western boundary of the GoT. Complex correlation between the total and geostrophic current is calculated to determine the correlation and phase relationship between the two velocity fields (Figure 6). Over the entire basin, the rms correlation coefficient is 0.70 (Figure 6a). The correlation between the total and geostrophic current is higher along the southern boundary of the observing domain, at 8° N. Along the northeastern boundary, geostrophic current only explains a small fraction of the total variance (14 − 34%). The rms correlation coefficient over the interior is 0.71, while those averaged over the uGoT and the western boundary are lower with values of 0.63 and 0.67, respectively. The strong correlation indicates the dominance of geostrophic circulation over the GoT. Phase relationship shows the direction that the geostrophic current has to rotate to align with the direction of the total current where positive denotes counterclockwise rotation.In the central and lower GoT (south of 12° N), a negative phase relationship is found roughly to the north of 10.5° N while a positive relationship is found to the south of 10.5° N (Figure 6b). With the dominating anticyclonic circulation centered at 10.5°-11° N during the southwest monsoon and fall monsoon transition, the phase relationship requires southeastward ageostrophic flow. In contrast, the phase relationship implies northwestward ageostrophic current during the northeast monsoon and spring monsoon transition when cyclonic circulation dominates. As the prevailing monsoon wind is southwesterly during the southwest monsoon and northeasterly during the northeast monsoon, the resulting wind-driven Ekman current aligns with the direction of the ageostrophic flow in the respective seasons. This reflects the importance of the wind-driven Ekman flow on the GoT circulation, although the Ekman velocity averaged in the upper 30 m of the water column (or to the seafloor where the water column is shallower than 30 m) computed from the CCMPv2 wind is generally smaller than the ageostrophic current. The rms of monthly wind-driven Ekman current ranges from 0.01 to 0.05 m s^{-1} with a similar range in median (Figure 4b, d, f, h).

In the uGoT, the correlation coefficient between the geostrophic and total currents is also high and significant with 95% confidence (Figure 6a). The phase relationship is mainly positive (Figure 6b) indicating westward (northward) ageostrophic current during the southwest (northeast) monsoon. During the fall monsoon transition, the positive phase relationship implies southward ageostrophic current. Compared to results from a numerical study which indicates circulation in the direction of the expected wind-driven current over the uGoT (i.e. anticyclonic during the southwest monsoon and cyclonic during the northeast

monsoon) (Buranatheprat et al., 2002), the circulation based on the remotely sensed observations is not quite consistent. The
190   inconsistency could reflect forcings neglected by the numerical simulation that is included in the remotely sensed observation,
e.g. the spatially-variant wind pattern and form drag (MacCready et al., 2003). Also, the difference in circulation patterns could
be attributed to the insufficient spatial resolution of the observations over such a small area with shallow bathymetry. During
the spring monsoon transition, the ageostrophic current is northward in the same direction to that of the wind-driven Ekman
current, although the calculated wind-driven current is smaller than the ageostrophic current (Figure 4b).

195

Complex correlation between the ageostrophic component and wind-driven Ekman current is calculated to examine the con-
tribution of wind-driven current on the ageostrophic circulation (Figure 6c). Higher correlation is found over the southern part
of the domain with the highest correlation coefficient of 0.54 reflecting that up to 29% of the ageostrophic circulation is wind-
driven. Over the western boundary region, the correlation coefficient between the wind-driven current and the ageostrophic
200   current is 0.40. Similar value of correlation coefficient is observed over the interior of the GoT ($r = 0.41$). The uGoT is one
of the regions where the wind-driven current only explains a small percentage of total variance in ageostrophic flow; $r = 0.20$,
significant with 95% confidence. Phase relationship indicates the direction that the Ekman current has to rotate to align with the
direction of the ageostrophic current; it is small overall with most values between $-\frac{\pi}{4}$ and $\frac{\pi}{4}$ (Figure 6d). When ageostrophic
current is entirely driven by wind stress, the phase relationship is zero. Thus, the small phase relationship hints the importance
205   of forcings other than wind stress on ageostrophic current, e.g. counterflow produced by the bottom friction (the bottom Ekman
layer), etc. Negative phase is only found in a narrow band along the northwestern boundary reflecting that wind-driven current
is to the left of ageostrophic flow. The negative phase is clearly evident in June and December when monsoon winds are strong,
while it is not clear during the monsoon transitions (March and September) (Figure 4a-d).

3.1.3   The role of wind stress curl on the sea surface height

210   The impact of the wind stress curl on sea surface height is examined through a linear regression using daily measurements.
The basin-averaged wind stress curl and ADT have distinct seasonal cycle consistent with water level measurements from tide
gauges (Trisirisatayawong et al., 2011); high (low) ADT is observed during the northeast (southwest) monsoon over the entire
basin, while the wind stress curl exhibits the opposite pattern (Figure 7a). In addition, the intraseasonal signals of the basin-
averaged ADT covary quite well with the basin-averaged wind stress curl. The anticorrelation yields a significant negative
215   correlation of -0.84 reflecting the dominance of wind stress curl on the ADT through local Ekman pumping; positive (negative)
wind stress curl induces upward (downward) flow in the water column and depresses (raises) the ADT. The high anticorrelation
reflects the instantaneous adjustment of the ADT as being forced by the local wind stress curl. As Zhou et al. (2012) suggest
a delayed response of the ADT to wind stress curl over the SCS (decaying timescale of 40 days), the result demonstrates the
different wind-associated dynamic that underlies the GoT compared to the rest of the SCS.

220

As most energy of the GoT circulation locates along the western boundary of the GoT (Figure 2, 3, 4), the influence of wind
stress curl on current variability at 9.6° N, 99.9° E representing high ADT variance in the uGoT (purple cross in Figure 2b) and

12.9° N, 100.1° E representing high variance along the western central GoT (green cross in Figure 2b) are further investigated. Correlation coefficient is calculated between ADT at each selected location and wind stress curl over the entire GoT to identify

225 the location of wind stress curl that influences the ADT. ADT with high variance over the uGoT correlates well with wind stress curl over the uGoT with a correlation coefficient of -0.80 suggesting a local response of ADT and thus the geostrophic current on the wind stress curl, although much of the correlation attributes to the dominant seasonal cycle observed in both variables (Figure 2b, 7c). However, high-variance ADT at the western boundary is correlated with wind stress curl 280 km to its north (Figure 2b, 7b). Wind stress curl to the south of uGoT (12.1° N, 100.1° E) explains 80% of the ADT variance at the central

230 part of the GoT western boundary (9.6° N, 99.9° E) as it also captures intraseasonal fluctuation of the ADT. The mechanism associated with high correlation between ADT at the western boundary and remote wind stress curl is still unclear and beyond the scope of this study. Still, the result suggests the importance of coastal trapped Kelvin waves which travel equatorward along the western boundary of the basin. At the GoT interior, wind stress curl does not exhibit seasonal cycle, and thus, the local wind stress curl does not locally influence the ADT there.

235 ## 3.2 Interannual variability of the circulation in the Gulf of Thailand

The influences of ENSO and IOD are examined to understand interannual variability of the GoT circulation. Low-frequency OSCAR velocity is calculated by removing the seasonal cycle, taken as a linear combination of annual and semiannual harmonics that best fit the 6-year observations, and signals with periods shorter than 90 days. A 90-day lowpass filter is also applied to sea surface temperature averaged over the Niño 3.4 box (hereafter referred to as Niño3.4) which indicates ENSO

240 conditions and Dipole Mode Index (DMI) which indicates IOD conditions. Complex correlation between the low-frequency indices, which have a phase of zero ($\pm\pi$) for a positive (negative) value, and the low-frequency currents is calculated over the entire GoT (Figure 8a, b). The correlation shows fascinating patterns revealing that the ENSO conditions highly influence the circulation over the central and the eastern parts of the GoT, while IOD conditions influence the current along the western boundary of the GoT and the southern boundary of the observing domain.

245

The low-frequency zonal current averaged over the uGoT (12.5° - 13.5° N, 100.0° - 101.0° E) correlates with the low-frequency Niño3.4 with a correlation coefficient of -0.29 (significant at the 95% confidence level); the current is anomalously westward (eastward) during an El Niño (La Niña) event (Figure 9a). During the 2015/2016 El Niño, the area-averaged current anomaly is generally westward; still, the current anomaly fluctuates quite a bit which contributes to the low correlation. The

250 current is anomalously eastward during the 2017/2018 La Niña. To understand the dynamics associated with the low-frequency variability of the GoT circulation, correlations between low-frequency Niño3.4 and selected forcings, which are ADT, zonal wind stress, and wind stress curl, are calculated (Figure 8c, e, g). Similarly, those between DMI and the selected forcing are also computed (Figure 8d, f, h). Note that the meridional wind stress is also considered; however, its correlation with either of the indices does not exhibit a distinct variation pattern over the GoT. The mechanism associated with the low-frequency zonal

255 current variability over the uGoT during ENSO conditions is, however, unclear as the local low-frequency ADT, wind stress, and wind stress curl do not suggest a negative relationship between the current and Niño3.4. The correlation map implies a

positive ADT gradient anomaly eastward during an El Niño condition (Figure 8c), which is influenced by the local wind stress curl (Figure 8g), resulting in a northward current anomaly. The low-frequency zonal wind over the uGoT tends to be eastward producing a southeastward current anomaly (Figure 8e), while the meridional wind stress tends to be positive yielding a north-

260 eastward anomaly (not shown). During La Niña conditions, the uGoT current anomaly and anomalies of the selected forcings tend to reverse their direction. A higher and positive correlation of 0.39 is found between the area-averaged zonal current and DMI suggesting the tendency of eastward (westward) zonal current anomaly during a positive (negative) IOD phase (Figure 9a). The expected anomalous current pattern is observed during both the 2016 negative IOD and 2019 positive IOD events. The positive relationship is largely geostrophic as the low-frequency ADT gradient is positive southward (northward) over the

265 uGoT during an El Niño (a La Niña) producing eastward (westward) geostrophic current (Figure 8d). The ADT pattern is likely influenced by local wind stress curl as a positive curl lowers the ADT and a negative curl elevates it (Figure 8h). Note that the interannual meridional velocity averaged over the uGoT is also considered; however, it does not correlate well with the climate modes (not shown).

270 Along the western boundary of the GoT, high correlation between the low-frequency current and low-frequency DMI is found with a phase relationship of $\frac{\pi}{2}$ indicating northward (southward) current anomaly during a positive (negative) IOD condition (Figure 8b). The low-frequency alongshore current averaged in 9.0° - 11.5° N, 99.5° - 100.2° E region is used to represent the current along the western boundary; low-frequency DMI explains 45% of the variance of the alongshore meridional flow (Figure 9b). During the 2016 negative IOD event, the southward western boundary current (Figure 4) intensifies during the

275 southwest monsoon and fall monsoon transition. In contrast, the seasonal southward current significantly weakens during the southwest monsoon and fall monsoon transition of 2019 when a positive IOD occurs. The low-frequency variability of the current is likely associated with local zonal wind stress (Figure 8f). Low-frequency component of the zonal wind stress shows strong correlation with the DMI along the GoT western boundary with correlation coefficients of up to -0.75 and along the southern boundary of the domain with correlation coefficients of up to -0.58; the correlation pattern is similar to that between

280 OSCAR current and DMI (Figure 8b). The negative correlation suggests the westward (eastward) wind stress anomaly during a positive (negative) IOD event yielding a northwestward (southeastward) surface Ekman current anomaly along the western boundary, consistent with the low-frequency OSCAR current. Although the low-frequency wind stress curl and ADT also suggest northward flow anomaly along the western boundary, the influence is roughly the same along the entire western boundary as well as the eastern boundary (Figure 8d, f). Therefore, the low-frequency variability of the current along the GoT western

285 boundary is likely not associated with the ADT and wind stress curl variability during IOD conditions. Correlation between low-frequency Niño3.4 and low-frequency alongshore current is small ($r = 0.14$) but significant with 95% confidence suggesting a tendency of northward (southward) current anomaly during an El Niño (La Niña) event; however, the current anomaly is not clearly apparent during the 2015/2016 El Niño and the 2017/2018 La Niña (Figure 9b).

290 In the GoT interior, a region of high correlation between Niño3.4 and OSCAR current is found at 10.0° - 11.0° N, 100.5° - 103.0° E (the northern dashed box in Figure 8a), with the out-of-phase relationship that indicates westward current anomaly

during an El Niño event and eastward current anomaly during a La Niña event. Considering low-frequency zonal current averaged over the region, Niño3.4 explains 34% of the low-frequency variance of the zonal flow (Figure 9c). With a 75-day lag of the area-averaged current, the correlation improves to -0.71; half of the variance in low-frequency zonal current at this region

295   is associated with ENSO condition. Along the southern boundary of the domain (8° - 9° N, 101.5° - 104.0° E), the correlation is also high and significant with 95% confidence. However, the relationship is in-phase indicating an eastward (westward) current anomaly during an El Niño (a La Niña) event. The low-frequency Niño3.4 explains 14% of variance in the area-averaged low-frequency zonal current with no lag (Figure 9c). This opposing pattern suggests a cyclonic current anomaly in the GoT interior during an El Niño and an anticyclonic anomaly during a La Niña with its location further south than the seasonal cyclonic

300   and anticyclonic circulation (Figure 3, 4a, c). The low-frequency cyclonic (anticyclonic) circulation during an El Niño event (a La Niña) colocates with anomalously low (high) ADT suggesting the dominance of geostrophic flow response in the GoT interior to ENSO variability (Figure 8c). The mechanism setting up the low-frequency ADT variability is unclear; it cannot be explained by local wind stress and wind stress curl (Figure 8e, g) but might relate to the winter warm pool (Li et al., 2014). Still, the influence of low-frequency wind stress curl on the ADT through coastal trapped Kelvin waves cannot be eliminated.

305   The correlation map suggests negative (positive) wind stress curl at the GoT eastern boundary between 8.5° and 11.5° N during an El Niño (La Niña) creating positive (negative) ADT anomaly that could propagate northward in the form of coastal trapped Kelvin waves. The cyclonic circulation is clearly observed following the 2015/2016 El Niño, particularly during the 2015/2016 northeast monsoon and the 2016 spring monsoon transition (Figure 9c); the seasonal cyclonic eddy locates further south centered at 9.5° N, 102.0° E. Shortly after the peak of the 2017/2018 La Niña, an anticyclonic anomaly centered at the

310   same location develops (Figure 9c). The anticyclonic eddy anomaly in the GoT interior becomes more pronounced during the 2018 spring monsoon transition when the La Niña decays. The low-frequency DMI is significantly correlated with low-frequency zonal current in the interior. However, it explains less than 5% of the low-frequency zonal current variance and the general circulation pattern away from the western boundary and the uGoT do not show a significant deviation from the seasonal current during the negative IOD event in 2016 and positive IOD event in 2019 (Figure 8b, 9c), although Higuchi et al. (2020)

315   suggest an anomalous outflow at the entrance during the southwest monsoon of positive IOD events.

4   Conclusions

This study exploits the synergy of available remotely-sensed observations to understand variability of the GoT circulation under the influence of highly variable winds at the seasonal and interannual timescales. At the interannual timescale, surface circulation over the GoT responds to different climate modes differently. The current along the western boundary is more sensitive to

320   IOD conditions, while that in the GoT interior is more sensitive to ENSO conditions (Figure 8, 9). At the seasonal timescale, the observation reveals spontaneous adjustment of the basin-averaged ADT following basin-averaged wind stress curl signal that is different from the rest of the SCS (Zhou et al., 2012). Still, the associated mechanisms are different over different parts of the GoT (Figure 7). For example, the ADT at the southern part of the uGoT highly correlates with the local wind stress curl reflecting the influence of local Ekman pumping, while the ADT along the western boundary is highly related with the

325   wind stress curl to its north reflecting the influence of remote forcing. The ADT variability sets up the surface geostrophic flow
which accounts for approximately half of the surface current variability (Figure 4, 6). The ageostrophic current is significantly
explained by the Ekman current, although the portion being explained varies from one region to another. The Ekman current
accounts for a larger percentage of the ageostrophic flow along the western boundary and the GoT interior, particularly to the
south of 10° N, compared to region to the north of this latitude.

330

The OSCAR surface current product also reveals the seasonal reversing circulation pattern at the surface following the mon-
soon wind reversal that accounts for 28% of the total current variance over the 2014 - 2019 period (Figure 3a-c). The seasonal
pattern confirms the anticyclonic circulation in the GoT interior with an outflow at the southeastern entrance during the south-
west monsoon (Figure 4) consistent with findings from Wyrtki (1961); Sojisuporn et al. (2010); Aschariyaphotha et al. (2008).

335   A cyclonic circulation along the western boundary of the GoT as suggested by a numerical simulation (Yanagi and Takao,
1998) is present but narrow, confined to the west of 100.5° E. Also, the western flank of the cyclonic circulation is stronger
than the eastern flank consistent with previous altimetric observation (Sojisuporn et al., 2010). During the northeast monsoon,
OSCAR product shows strong northward flow along the western boundary and an inflow at the southern entrance consistent
with observational (Sojisuporn et al., 2010) and numerical studies (Yanagi and Takao, 1998; Aschariyaphotha et al., 2008)

340   that suggest anticyclonic circulation over the GoT. However, the 6-year averaged surface velocity displays the dominance of
cyclonic circulation in the GoT interior (Figure 4), in agreement with that observed during the NAGA expedition (Wyrtki,
1961). As the uGoT is shallow and enclosed by land on the western, northern, and eastern sides, the derived surface circulation
could contain substantial error. Also, OSCAR observation is quite sparse in the uGoT and along the coastline; it does not fully
capture the complex circulation at these regions (Figure 1, 4). Therefore, finer resolution observations are critical to understand

345   the circulation pattern in the uGoT and along the coast.

Although this study offers insightful details of the GoT circulation, particularly to the south of 12.5° N, there are still forcings
that are not considered, for example, tidal currents and planetary waves. Previous studies have indicated the importance of tidal
pattern over the GoT that is different from one region to another (Yanagi and Takao, 1998) and is heavily dependent on tidal

350   pattern in the SCS (Cui et al., 2019). The effect of coastal trapped Kelvin waves on the coastal circulation which is also
observed in the nearby regions, e.g. the SCS and the East China Sea (Wang et al., 2003; Yin et al., 2014; Liu et al., 2011),
cannot be concluded despite the observed influence of remote wind stress curl on the western boundary current. Moreover,
the interaction between the SCS and GoT is still unknown. Thus, examination of these factors could further improve the
understanding of dynamics associated with the GoT circulation.

355   *Data availability.* The OSCAR third degree Version 1 data are provided by Physical Oceanography Distributed Active Archive Center.
CCMP Version-2.0 vector wind analyses available at www.remss.com are produced by Remote Sensing Systems. This study has been con-

ducted using E.U. Copernicus Marine ServiceInformation (http://marine.copernicus.eu/services-portfolio/access-to-products/?option=com_csw&view
=details&product_id=SEALEVEL_GLO_PHY_L4_REP_OBSERVATIONS_008_047).

Author contributions. The author confirms contribution to the paper as follows: data collection: A. Anutaliya; data analysis: A. Anutaliya;
360   discussion of results: A. Anutaliya.

Competing interests. The author declares no relevant competing interests.

Acknowledgements. This work has been supported by the 2021 Research Grant of Burapha University under grant 001/2564 to Arachaporn
Anutaliya.

References

365   Alberty, M., Sprintall, J., MacKinnon, J., Germineaud, C., Cravatte, S., and Ganachaud, A.: Moored Observations of Transport in the Solomon Sea, J. Geophys. Res. Oceans, 124(11), 8166–8192, 2019.

Aschariyaphotha, N. and Wongwises, S.: Simulations of Seasonal Current Circulations and Its Variabilities Forced by Runoff from Freshwater in the Gulf of Thailand, Arab. J. Sci. Eng., 37(5), 1389–1404, 2012.

Aschariyaphotha, N., Wongwises, P., Wongwises, S., Humphries, U. W., and You, X.: Simulation of Seasonal Circulations and Thermohaline
370   Variabilities in the Gulf of Thailand, Ad. Atoms. Sci., 25(3), 489–506, 2008.

Bonjean, F. and Lagerloef, G. S. E.: Diagnostic Model and Analysis of the Surface Currents in the Tropical Pacific Ocean, J. Phys. Oceanogr., 32, 2938–2954, 2002.

Buranatheprat, A., Yanagi, T., and Sawangwong, P.: Seasonal Variations in circulation and Salinity Distributions in the Upper Gulf of Thailand, La mer, 40, 147–155, 2002.

375   Buranatheprat, A., Yanagi, T., and Matsumura, S.: Seasonal variation in water column conditions in the upper Gulf of Thailand, Cont. Shelf Res., 28, 1509–2522, 2008.

Cui, X., Fang, G., and Wu, D.: Tidal resonance in the Gulf of Thailand, Ocean Science, 15(2), 321–331, 2019.

Ducet, N., Traon, P. Y. L., and Reverdin, G.: Global high-resolution mapping of ocean circulation from TOPEX/Poseidon and ERS-1 and -2, J. Geophys. Res., 105, 19 477–19 498, 2000.

380   Higuchi, M., Anongponyoshun, M., Phaksopa, J., and Onishi, H.: Influence of monsoon-forced Ekman transport on sea surface height in the Gulf of Thailand, Agr. Nat. Resour., 54, 205–210, https://doi.org/10.34044/j.anres.2020.54.2.12, 2020.

Holgate, S. J., Matthews, A., Woodworth, P. L., Rickards, L. J., Tamisiea, M. E., Bradshaw, E., Foden, P. R., Gordon, K. M., Jevrejeva, S., and Pugh, J.: New Data Systems and Products at the Permanent Service for Mean Sea Level, J. of Coastal Res., 29(3), 493–504, https://doi.org/10.2112/JCOASTRES-D-12-00175.1, 2013.

385   Kubryakov, A. A. and Stanichny, S. V.: Estimating the quality of the retrieval of the surface geostrophic circulation of the Black Sea by satellite altimetry data based on validation with drifting buoy measurements, Izv. Atmos. Ocean. Phys., 490, 930–938, 2013.

Li, J., Zhang, R., Ling, Z., Bo, W., and Liu, Y.: Effects of Cardamom Mountains on the formation of the winter warm pool in the Gulf of Thailand, Cont. Shelf Res., 91, 211–219, 2014.

Liu, Q., Feng, M., and Wang, D.: ENSO-induced interannual variability in the southeastern South China Sea, Journal of Oceanography, 67,
390   127–133, https://doi.org/10.1007/s10872-011-0002-y, 2011.

MacCready, P., Pawlak, G., Edwards, K., and McCabe, R.: Form drag on ocean flows, in: Proceedings of the 13th "Aha Huliko"a Hawaiian Winter Workshop: Near-Boundary Processes and their Parameterization, pp. 119–130, University of Hawaii at Monoa, Honolulu, HI, 2003.

Poulain, P.-M., Menna, M., and Mauri, E.: Surface Geostrophic Circulation of the Mediterranean Sea Derived from Drifter and Satellite
395   Altimeter Data, Journal of Physical Oceanography, 42, 973 – 990, https://doi.org/10.1175/JPO-D-11-0159.1, 2012.

PSMSL: "Tide Gauge Data", http://www.psmsl.org/data/obtaining/, 2019.

Saji, N. H., Goswami, B. N., Vinayachandran, P. N., and Yamagata, T.: A dipole in the tropical Indian Ocean, Nature, 401, 360–363, 1999.

Saramul, S.: Seasonal Monsoon Variations in Surface Currents in the Gulf of Thailand Revealed by High Frequency Radar, Eng. J., 21(4), 25–37, 2017.

400 Saramul, S. and Ezer, T.: On the dynamics of low latitude, wide and shallow coastal system: numerical simulations of the Upper Gulf of
     Thailand, Ocean Dyn., 64, 557–571, 2014.

Sojisuporn, P., Morimoto, A., and Yanagi, T.: Seasonal variation of sea surface current in the Gulf of Thailand, Coast. Mar. Sci., 34(1),
     91–102, 2010.

Sriwoon, R., Pholpunthin, P., Kishino, M., and Furuya, K.: Population dynamics of green Noctiluca scintillans (Dinophyceae) associated with
405   the monsoon cycle in the upper Gulf of Thailand, Journal of Phycology, 44, 605 – 615, https://doi.org/10.1111/j.1529-8817.2008.00516.x,
     2008.

Suvapepun, S.: Long term ecological changes in the Gulf of Thailand, Marine Pollution Bulletin, 23, 213–217,
     https://doi.org/https://doi.org/10.1016/0025-326X(91)90677-K, environmental Management and Appropriate Use of Enclosed Coastal
     Seas, 1991.

410 Trisirisatayawong, I., Naeije, M., Simons, W., and Fenoglio-Marc, L.: Sea level change in the Gulf of Thailand from GPS-corrected tide
     gauge data and multi-satellite altimetry, Global Planet. Change, 76, 137–151, 2011.

Wang, D., Wang, W., Shi, P., Guo, P., and Gan, Z.: Establishment and adjustment of monsoon-driven circulation in the South China Sea,
     Science in China Series D: Earth Sciences, 46, 173–181, https://doi.org/10.1360/03yd9016, 2003.

Wentz, F. J., Scott, J., Hoffman, R., Leidner, M., Atlas, R., and Ardizzone, J.: Remote Sensing Systems Cross-Calibrated Multi-Platform
415   (CCMP) 6-hourly ocean vector wind analysis product on 0.25 deg grid, Version 2.0, 2012-2017. Remote Sensing Systems, Santa Rosa,
     CA, www.remss.com/measurements/ccmp, 2015.

Wyrtki, K.: Scientific Results of marine investigations of the South China Sea and the Gulf of Thailand 1959–1961, Tech. Rep. 164-169,
     University of California at San Diego, 1961.

Yanagi, T. and Takao, T.: Clockwise Phase Propagation of Semi-Diurnal Tides in the Gulf of Thailand, J. Oceanogr., 54, 143–150, 1998.

420 Yanagi, T., Sachoemar, S. I., Takao, T., and Fujiwara, S.: Seasonal Variation of Stratification in the Gulf of Thailand, J. Oceanogr., 57,
     461–470, 2001.

Yin, L., Qiao, F., and Zheng, Q.: Coastal-Trapped Waves in the East China Sea Observed by a Mooring Array in Winter 2006, Journal of
     Physical Oceanography, 44, 576 – 590, https://doi.org/10.1175/JPO-D-13-07.1, 2014.

Yu, Y., Emery, W. J., and Leben, R. R.: Satellite altimeter derived geostrophic currents in the western tropical Pacific during
425   1992–1993 and their validation with drifting buoy trajectories, Journal of Geophysical Research: Oceans, 100, 25 069–25 085,
     https://doi.org/https://doi.org/10.1029/95JC02146, 1995.

Zhou, J., Li, P., and Yu, H.: Characteristics and mechanisms of sea surface height in the South China Sea, Glob. Planet. Change, 88-89,
     20–31, 2012.
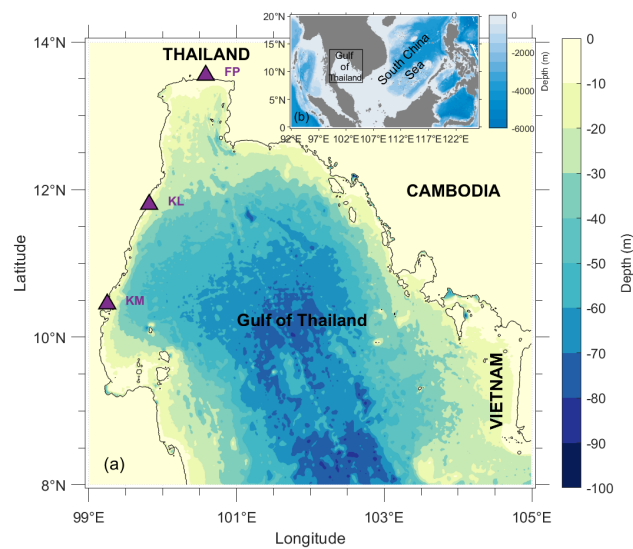
Figure 1. Map of the Gulf of Thailand with the locations of tide gauges (triangle): FP denotes Fort Phrachula Chomklao station, KL denotes Ko Lak station, and KM denotes Ko Mattaphon station (a) and the nearby regions (b). Color contour represents bathymetry and black contour represents the zero-depth level.
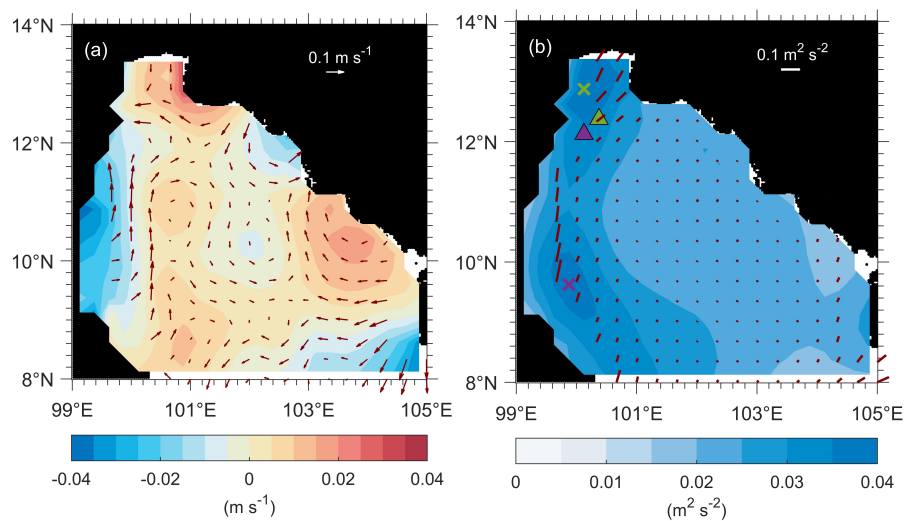
Figure 2. The 2014-2019 mean OSCAR current (maroon quivers) and ADT (color contour) over the Gulf of Thailand (a) and the OSCAR current variance (maroon) where the zonal component of the maroon line indicates variance of the zonal OSCAR current and the meridional component indicates variance of the meridional OSCAR current and ADT variance (color contour; b). Crosses in (b) mark locations with high ADT variance in the uGoT (green) and the western central GoT (purple) and the triangles with respective colors mark the locations of wind stress curls that correlate the best with the ADT shown in Figure 7.
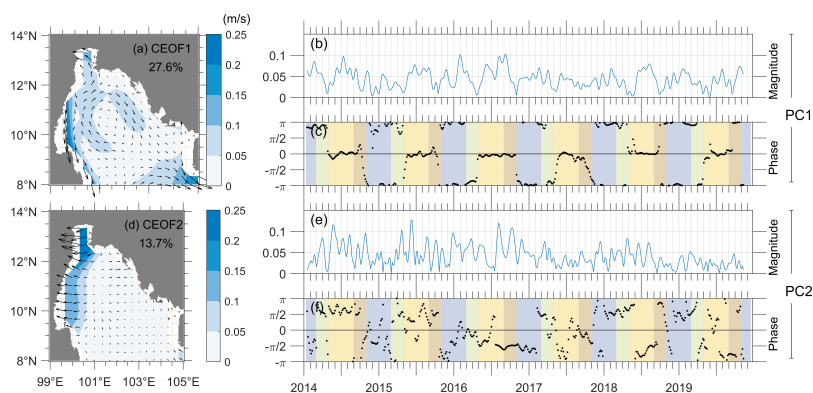
Figure 3. The first (a) and second (d) dominant complex empirical orthogonal function (CEOF) modes of the OSCAR current with the corresponding magnitudes (b), (e) and phases (c), (f) of the principal components (PC). Percentage of the current variance explained by each mode is shown on the upper right corner of (a) and (d). Maroon boxes in (a) and (d) designate the upper Gulf of Thailand region (the northern-most box), the western boundary region (the western-most box), and the Gulf of Thailand interior region (the eastern-most box). Background shading in (c) and (f) denotes different seasons: northern monsoon (blue), spring monsoon transition (green), southwest monsoon (yellow), and fall monsoon transition (brown).
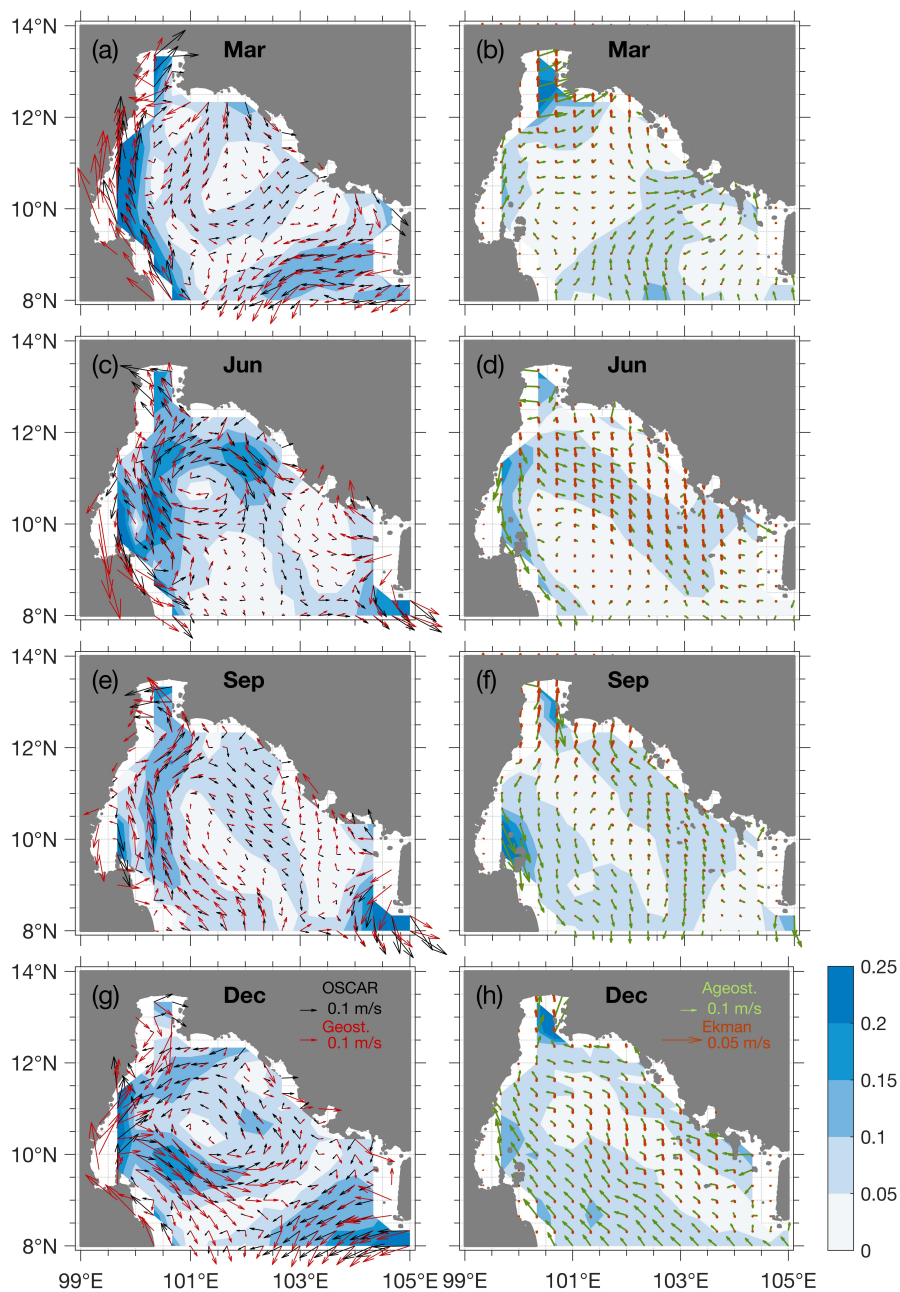
Figure 4. The 2014 - 2019 monthly mean OSCAR current (black; left column), geostrophic current estimated from satellite altimetry (red; left column), ageostrophic flow (green; right column), and wind driven Ekman current (brown; right column) over the Gulf of Thailand in March representing the spring monsoon transition (a) and (b), June representing the southwest monsoon (c) and (d), September representing the fall monsoon transition (e) and (f), and December representing the northeast monsoon (g) and (h). The color contour shown in subplots on the right (left) column indicates magnitude of the OSCAR (ageostrophic) current and the scale for the current is shown on the upper right corner of (g) and (h).
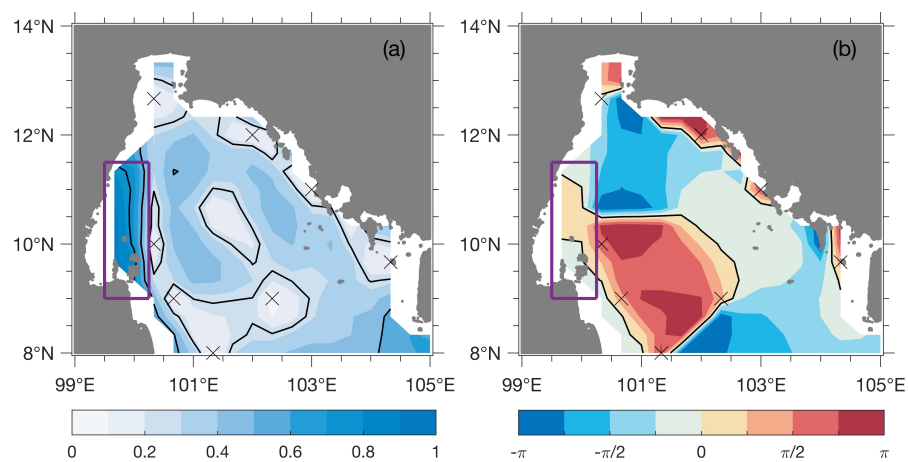
Figure 5. Complex correlation between OSCAR current along the western boundary (purple box) and OSCAR current over the entire Gulf of Thailand (a) and the corresponding phase (b). Black contour in (a) is plotted every 0.25 and that in (b) is plotted at 0 and π. Crosses indicate the regions where the correlation is not significant with the 95% confidence.
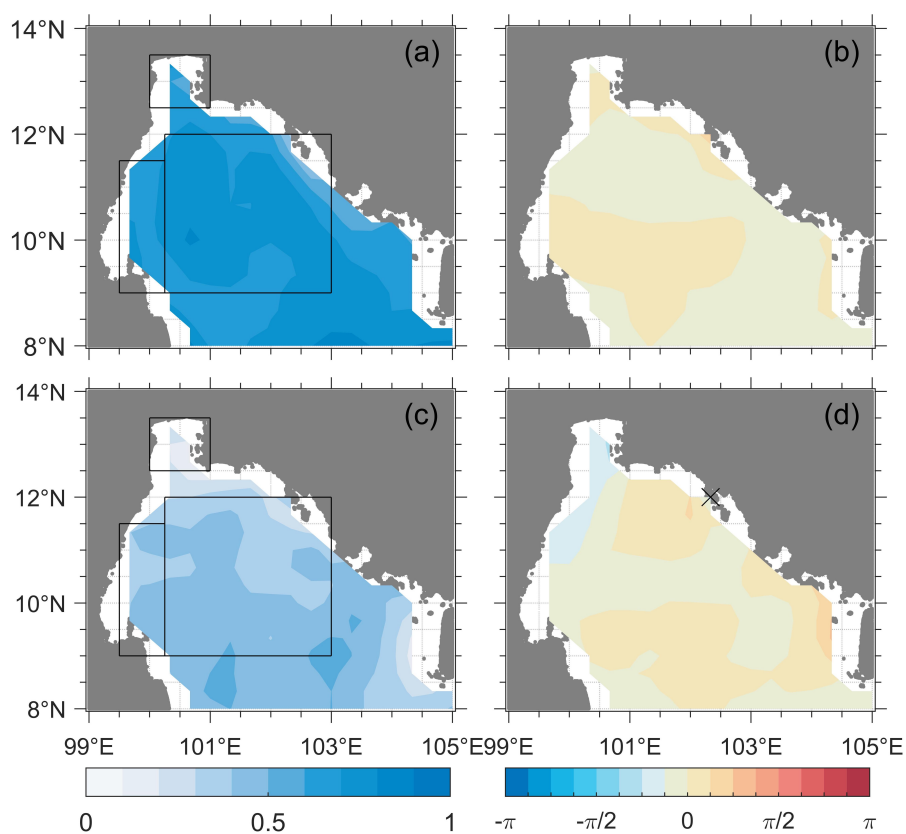
Figure 6. Complex correlation map between the OSCAR current and altimetry-derived geostrophic current (a) and that between ageostrophic current and the Ekman current (c) with the respective phase shown in (b) and (d).
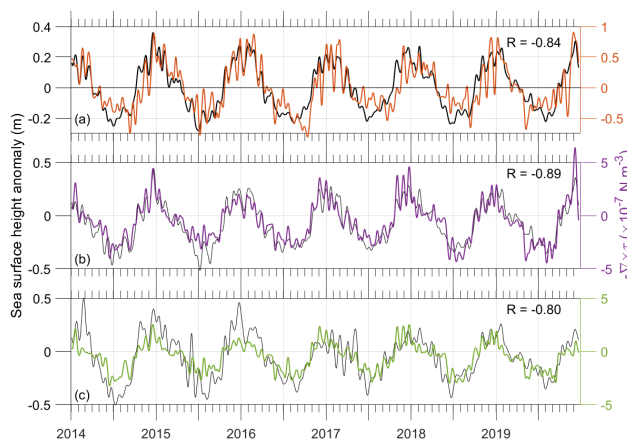
Figure 7. Comparison between sea surface height anomaly (black) and negative wind stress curl (colors): both sea surface height anomaly (black) and wind stress curl (orange) averaged over the entire Gulf of Thailand (a), sea surface height anomaly (black) at the Gulf of Thailand western boundary shown as purple cross in Figure 2b and wind stress curl (purple) to the south of the upper Gulf of Thailand shown as purple triangle in Figure 2b (b), and both sea surface height anomaly (black) and wind stress curl (green) to the south of the upper Gulf of Thailand shown as green cross and triangle in Figure 2b (c). Correlation coefficient between each comparison is shown on the upper right corner of each subplot.
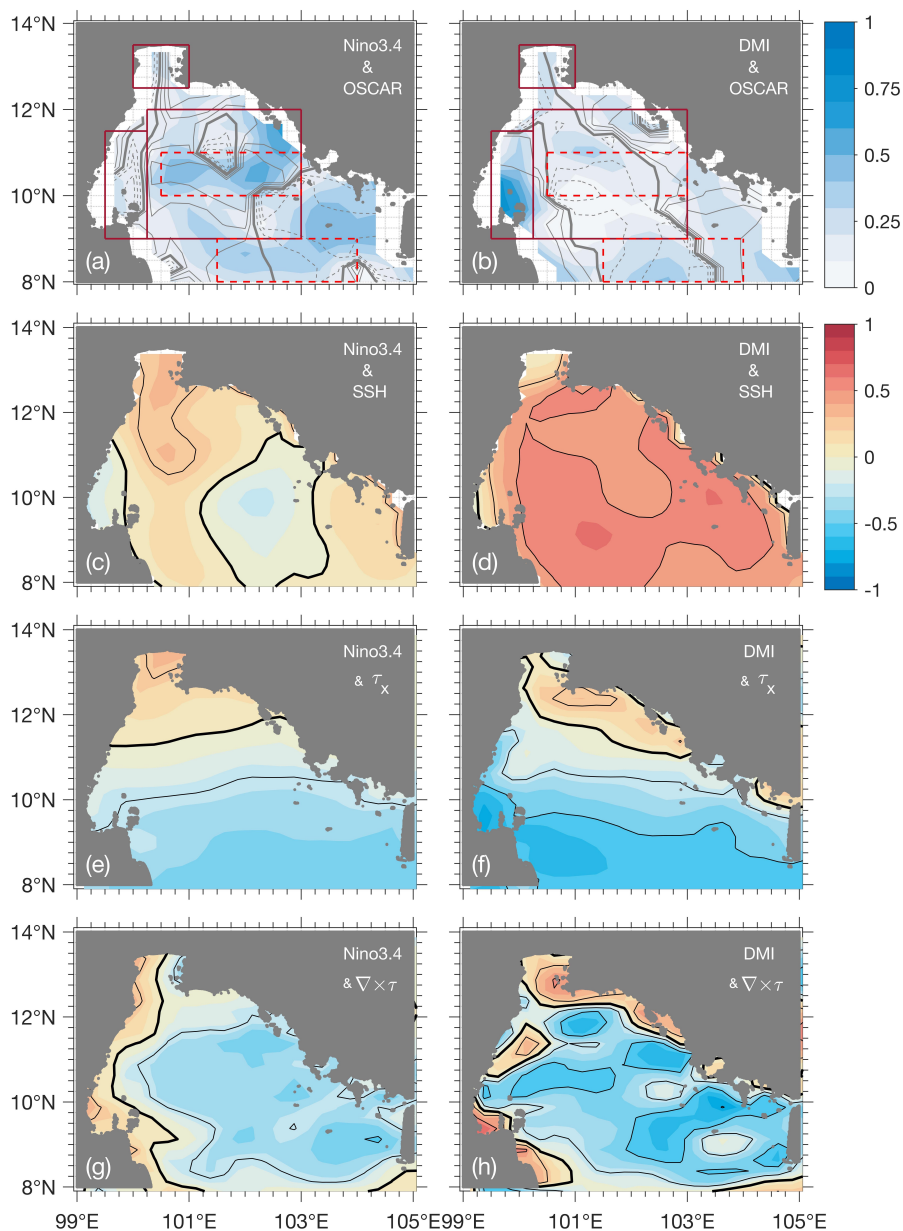
Figure 8. Correlation maps between the Niño 3.4 index and OSCAR current (a), sea surface height (c), zonal wind stress (e), wind stress curl (g), and those between the Dipole Mode Index and OSCAR current (b), sea surface height (d), zonal wind stress (f), wind stress curl (h). Gray contour in (a) and (b) shows the phase associated with the complex correlation map. Solid (dashed) gray line is plotted every $\frac{\pi}{4}$ showing the positive (negative) phase relationship and thick gray line shows the zero contour. The maroon boxes in (a) and (b) designate the upper Gulf of Thailand region (the northernmost box), the western boundary region (the western-most box), and the Gulf of Thailand interior region (the easternmost box). Dashed maroon boxes are areas that show high low-frequency variability used in 9c. Thick black contour in (c) – (h) denotes 0 and thin black contour is plotted every 0.25.
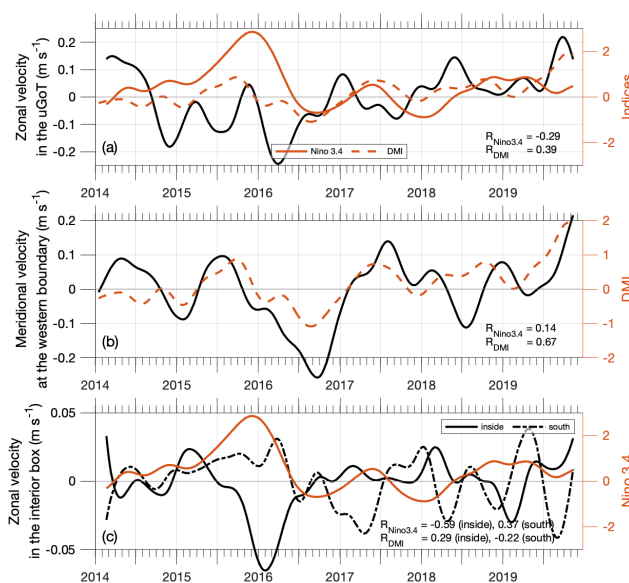
Figure 9. The low-frequency current (black line) representing circulation in the selected regions shown in Figure 8a: mean zonal velocity in the upper Gulf of Thailand (a), mean meridional velocity at the western boundary (b), and mean zonal velocity in the middle of the interior box (solid) and to the south of the box (dashed) (c), and the low-frequency climate modes: Niño 3.4 index (solid orange line) and Dipole Mode Index (dashed orange line). Only the climate mode index that shows higher correlation is shown in subplot (b) and (c). Correlation coefficients between the current and both climate modes are shown on the lower right corner of each subplot; the correlation coefficients between the climate modes and the mean zonal velocity in the middle of interior box are shown as the first values and those with the mean zonal current to the south of the box are shown as the second values.